2

A FINITE ELEMENT METHOD FOR COMPOSITE SCATTERERS

A. H. J. Fleming

2.1 Introduction

Due to the practical importance and difficulties associated with their closed form solutions, the experimental and computational study of conical antennas and scatterers, such as sphere-cones, round and flat-based and loaded bicones [1,2] has been closely connected with the evolution of numerical methods in electromagnetics. During the past two decades, the widespread use of such methods has allowed a broad range of important scattering problems involving non-standard shapes, boundary conditions and material composition to be solved. While computing speed and the availability of central memory remain

a hurdle, interest in ever more complex processes provides a major driving force as instanced by recent studies involving composite objects [3–5].

The purpose of this chapter is to outline a differential method for the solution of composite scattering problems. In this section, we briefly survey some current problem types and solution methods. Section 2.2 discusses the unimoment technique [6] and the axisymmetric coupled azimuthal potentials (CAPs) [7]. Section 2.3 details the subsequent numerical procedure including the finite element method, the mesh and linear equation solver. The procedure is validated using standard Mei series calculations for spheres. In section 2.4, further tests of the method are performed using some standard shaped loaded and unloaded scatterers. Next, experimental results obtained from monostatic measurements are compared with computations for a series of loaded bicones. In Section 2.5, some conclusions are made about the procedure with particular regard for the method of incorporating conductors. Finally, some developments of the concepts of the CAP/unimoment method are discussed in Section 2.6.

Due to the computational economies afforded, bodies of revolution (BORs) or axisymmetric objects as illustrated in Fig. 1 have been the basis of many studies. The incident and impressed fields are not in general axisymmetric although they are azimuthally continuous and thus amenable to Fourier analysis. In order to get an approximate quantitative understanding of a complicated phenomenon such as microwave frequency hot spots in the human cranium, axisymmetry has been assumed [8]. Many problems remain however concerning essentially non-axisymmetric objects [9] while future composite studies such as therapeutic applicators promise to be most worthwhile [10].

Two major types of numerical method have been employed to date to solve scattering in the Rayleigh or resonance region via Maxwell's equations and associated boundary conditions, namely integral equation and differential equation methods. The two can be related by successively integrating by parts [11]. There are fundamental differences that make either method more appropriate for different applications. Integral equations distribute the sources over surfaces (2-D manifolds) so that the surface element intercoupling falls off relatively slowly with distance, generally resulting in dense matrices. However, since radiation conditions are incorporated as limits of integration, infinite regions are easily handled. On the other hand, differential methods give a description at each point in terms of the fields at the surrounding set

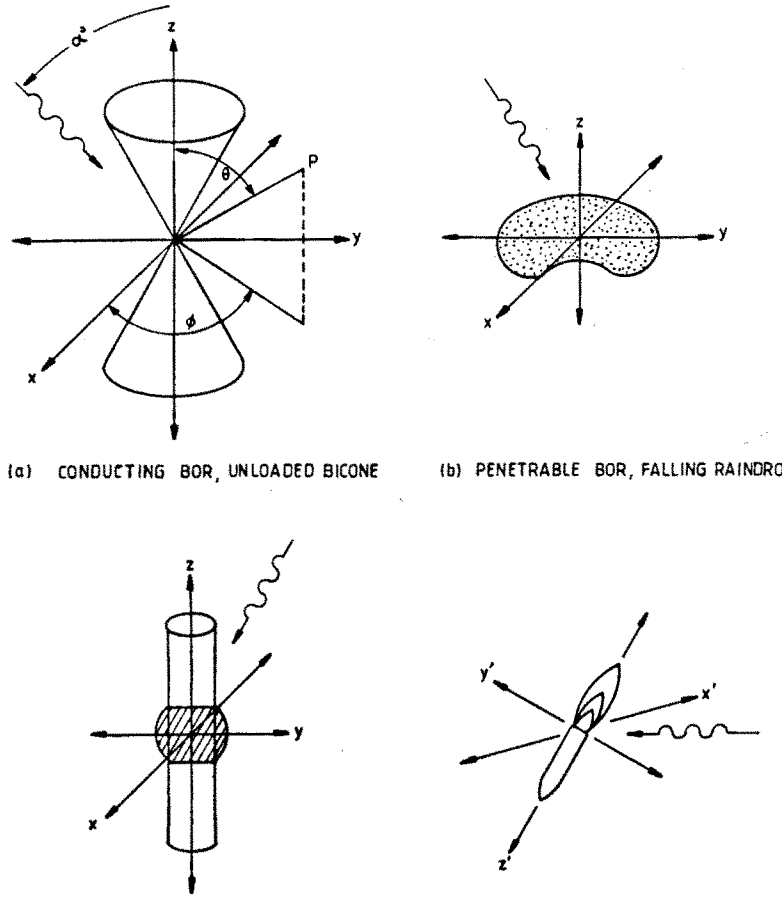

Figure 1 Various axisymmetric scattering problems.

of nodes in a volume (3-D manifold). This provides a more localized effect, resulting in sparse matrices. Some means of coupling the differential method to the exterior infinite region is required however.

Integral equation methods which utilize the surface equivalence principle are most effective for applications involving piecewise homogeneous regions [12,13]. The missile plume problem (Fig. 1) was treated as a layered dielectric with a conducting inside surface [3]. Use of the moment method results in a block tridiagonal matrix consisting

of dense submatrices. Recently, a comparison was made of different surface integral equation (SIE) formulations as applied to coated conductors [4]. At each surface, either electric or magnetic equivalent surface currents may be used, or both may be combined. The advantage of using single source formulations is the reduction in the required number of variables. Difficulties arise however depending upon whether or not associated over-constraints are satisfied. Thus at each single source layer surface, the solution can be affected by uniqueness problems at interior resonances when the permittivity of the coating is large.

Integral equation methods can be used for continuously inhomogeneous regions. A volume integral equation utilizing the polarization currents inside a volume and equivalent surface currents on an enclosing boundary surface can be formulated [14,15]. Three current components are required to be solved at each node in the volume. Thus the matrix, which is of order $3n^3$ where n is the number of nodes in the volume, becomes large for anything other than a coarse grid.

Where continuously varying inhomogeneities are present, such as biological systems, a differential method is appropriate. Furthermore, where inter-regional surfaces involve sharp reentrant angles, a numerical method based on differential equations accounts for the rapidly changing field solution near the cusp in a more direct manner; the mesh density is increased near the point. With the SIE approach, special care must be taken with the equations of continuity at such points.

Two differential methods, finite differences and finite elements have been used. With the finite difference method, approximate partial differences are applied directly to the field equations while the finite element method uses a weighting procedure to obtain a system of derived equations in which the errors are more evenly distributed throughout the problem domain.

While several techniques exist for coupling differential methods to the exterior region, such as infinite elements [16], *ballooning* [17] or the field feedback formulation [18], one effective means is the unimoment method [6]. Together with the unimoment method, the axisymmetric CAPs have been used to analyze structurally axisymmetric scattering, radiation, penetration and absorption problems. The CAP/unimoment formulation has proved over the past decade both powerful and flexible. Some applications have involved lossy dielectric objects [8,19,20]. Other extensions and hybrid techniques have been used [21,22]. Recently, the CAP equations were allied with the field

feedback formulation to analyse thin dipoles [18].

Stovall and Mei [2] studied radiation from loaded bicones using the finite difference method allied with the unimoment method and a symmetric form of the CAPs which results in a single potential. No account as to the end shape of the bicone was taken. The present study was initiated in part to examine the effect of shifting the surface of the unimoment method outwards and thus allow the analysis of various composite antenna structures. It was considered that this shifting of the unimoment method surface might also avoid possible continuity complications at the cone-hemisphere junction.

A finite element method based on the theory of the axisymmetric CAPs was used together with a conductor surface skin model which was included in the finite element mesh. This part of the mesh which approximates the field distributions at an imperfect conductor surface was used instead of applying perfect conductor boundary conditions. The important parameters were found to be the conductivity of the skin region and the ratio of the internal nodal separation (the mesh density) to that used external to the conductor. Reducing the size of the mesh as it proceeds radially inside the conductor surface accounts for the large wave numbers inside the skin.

2.2 Formulation

The following formulation is specialized to bodies of revolution, but could be generalized to arbitrary 3-D inhomogeneous structures. The unimoment method is quite flexible and extensions of the CAP equations to piecewise axisymmetric, quasi-axisymmetric, and full 3-D have recently been suggested (see Chapter 6), [23].

We address a generic problem involving axisymmetric composite structures where the conducting region is assumed to enclose the origin of a normalized cylindrical coordinate system and the dielectric either totally or partially surrounds the internal metallic region. Biregional or triregional unimoment methods can be used to separate the inhomogeneity depending on the shape and nature of the conductor. In the inhomogeneous region, Maxwell's equations can be written as time-harmonic modal expansions (the axisymmetric CAP equations) appropriate for coupling to the free-space and core region spherical harmonics.

The inhomogeneities involve isotropic regions where the shape and

the constitutive parameters are both assumed to be rotationally invariant: $\epsilon(r,\theta) = \epsilon_0\epsilon_r(r,\theta); \mu(r,\theta) = \mu_0\mu_r(r,\theta)$.

a. *Unimoment Method*

For the general case of an arbitrarily shaped scatterer, the unimoment method [6] uses a series of boundary trial functions in order to numerically enforce electromagnetic continuity at a surface surrounding the inhomogeneous region of the object under analysis. As illustrated in Fig. 2, this region can be surrounded both internally and externally by homogeneous core and free-space regions. Care needs to be taken in the selection of the boundary trial functions which should form a complete polynomial set.

Savings are possible by choice of canonical surfaces which allow the reuse of computed modal expansions. Using the appropriate modal series at nodes on the canonical surface, C, either for the scattered, incident or interior fields, continuity of the total electromagnetic fields and their normal derivatives is sought. Use of modal boundary conditions along C for the interior fields automatically ensures modal and total field continuity along C. What is needed then is to obtain the mix of modal coefficients which also ensures normal derivative continuity.

This can be done by obtaining the field values along a congruent curve C', enabling the normal derivative to be numerically estimated by using field differences between the two curves. This can be inaccurate depending on how the gradient estimates are derived. A simpler more accurate method of obtaining the desired continuity between regions is to ensure the total fields are also matched along C'.

For coupling with the CAP formulation the surfaces which separate these regions can be of any shape that permit the convenient orthogonal separation of the azimuthal coordinate, ϕ , into the spectral modes, $e^{jm\phi}$. In the present application, spheres and spherical harmonics were used. Figure 3 shows in cross-section, a loaded dipole, the two spherical separable surfaces S_{HC} (homogeneous core) and S_F (free-space) and their congruents S_0 and S_1.

The modal azimuthal fields may be derived from

$$E_{\phi,m} = \frac{1}{j\omega\epsilon r\sin\theta}\frac{\partial^2 A_{r,m}}{\partial r\partial\phi} + \frac{1}{r}\frac{\partial F_{r,m}}{\partial\theta} \tag{1a}$$

$$H_{\phi,m} = \frac{1}{j\omega\mu r\sin\theta}\frac{\partial^2 F_{r,m}}{\partial r\partial\phi} - \frac{1}{r}\frac{\partial A_{r,m}}{\partial\theta} \tag{1b}$$

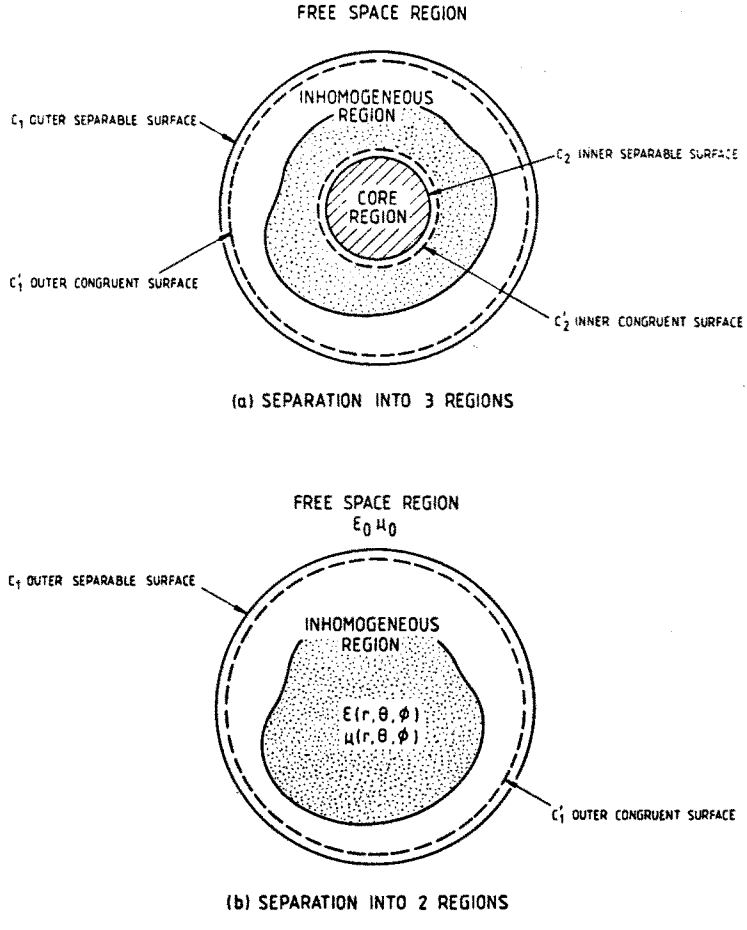

Figure 2 Unimoment surfaces: (a) Triregional and (b) Biregional.

with the radial electric and magnetic vector potentials given by

$$F_{r,m} = \frac{\sqrt{\mu_r}}{k_0} \sum_{n=m}^{N_m} a_{m\,n} P_n^m(\cos\theta) \hat{B}_n(kr) e^{jm\phi} \tag{1c}$$

$$A_{r,m} = \frac{\sqrt{\epsilon_r}}{\eta_0 k_0} \sum_{n=m}^{N_m} b_{m\,n} P_n^m(\cos\theta) \hat{B}_n(kr) e^{jm\phi} \tag{1d}$$

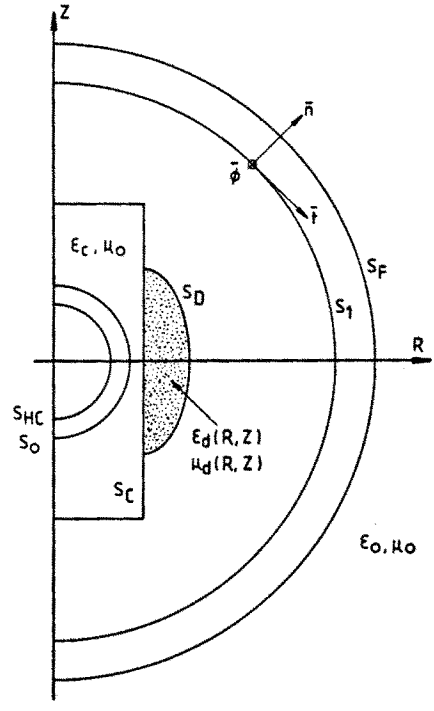

Figure 3 Semi-annular region for loaded dipole.

The complex propagation constant, in the assumed homogeneous material, is given by $k = \omega\sqrt{\mu\epsilon}$. Also, $\eta_0 = \sqrt{\mu_0/\epsilon_0} \approx 120\pi$ ohms, P_n^m are associated Legendre functions of the first kind, $\hat{B}_n$ are Riccati spherical Bessel functions, N_m is a truncation limit on the radial modal index, n, and m is the azimuthal modal index. The modal coefficients, a_{mn} and b_{mn}, are determined to numerically enforce continuity of the fields via the moment method.

While the above form of the unimoment method works well with nearly spherical objects, other three dimensional orthogonal systems may be used for other shapes, for instance thin wires, where spherical harmonics are inefficient and converge slowly. Similarly, objects such as the human body could be better modelled using spheroids and spheroidal harmonics.

b. Analytic CAP Formulation

The analytical derivation of the axisymmetric CAP formulation [24] begins by taking a Fourier series in the azimuthal coordinate ϕ, thus separating the azimuthal variable,

$$\overline{E}(R,Z,\phi) = \sum_{m=-\infty}^{\infty} \overline{e}_m(R,Z)e^{\jmath m\phi} \tag{2a}$$

$$\eta_0\overline{H}(R,Z,\phi) = \sum_{m=-\infty}^{\infty} \overline{h}_m(R,Z)e^{\jmath m\phi} \tag{2b}$$

The magnetic field is scaled by the free-space impedance, η_0, which simplifies the resulting coupled set of partial differential equations. Use of a normalized cylindrical coordinate system ($R = k_0\rho, Z = k_0 z$) enables the application of cartesian finite elements in the cross-sectional plane (r,θ).

In the inhomogeneous isotropic region, Maxwell's curl equations for time-harmonic, source free regions where conductive media may be present, are rewritten using equations $(2a-b)$. The resulting set of equations may be written in partitioned matrix form

$$\left[\begin{array}{cc|cc|cc}
\frac{\epsilon_r}{R} & 0 & 0 & -\jmath\frac{\partial}{\partial R} & 0 & \jmath\frac{\partial}{\partial Z} \\
0 & \frac{\mu_r}{R} & -\jmath\frac{\partial}{\partial Z} & 0 & \jmath\frac{\partial}{\partial R} & 0 \\
\hline
0 & \jmath\frac{\partial}{\partial Z} & -R\epsilon_r & m & 0 & 0 \\
\jmath\frac{\partial}{\partial R} & 0 & m & -R\mu_r & 0 & 0 \\
\hline
0 & \jmath\frac{\partial}{\partial R} & 0 & 0 & R\epsilon_r & m \\
\jmath\frac{\partial}{\partial Z} & 0 & 0 & 0 & m & R\mu_r
\end{array}\right]
\left[\begin{array}{c}
\psi_{1,m} \\ \psi_{2,m} \\ \hline e_{R,m} \\ h_{Z,m} \\ \hline e_{Z,m} \\ h_{R,m}
\end{array}\right]
=
\left[\begin{array}{c}
0 \\ 0 \\ \hline 0 \\ 0 \\ \hline 0 \\ 0
\end{array}\right] \tag{3}$$

where $e^{\jmath m\phi}$ terms have been omitted and the modal CAP variables $\psi_{1,m}$ and $\psi_{2,m}$ are defined in terms of the azimuthal modal field components, $e_{\phi,m}$ and $h_{\phi,m}$.

$$\psi_{1,m} = R\, e_{\phi,m} \tag{4a}$$

$$\psi_{2,m} = R\, h_{\phi,m} \tag{4b}$$

The 6 × 6 system of modal equations in (3) is seen to be block-reducible and any of the three pairings indicated can be used to convert these first order equations into an equivalent system involving only a collapsed 2×2 set of coupled second order partial differential equations.

For the axisymmetric structures involved, the CAP variables, $\psi_{1,m}$ and $\psi_{2,m}$, are continuous everywhere. This is so at all source-free cross-sectional junctions, even across conductor and dielectric interfaces. Naturally, field components in the cross-sectional plane normal to the CAPs may be discontinuous. Choosing the CAPs as problem variables results in the following 2 × 2 coupled system of partial differential equations:

$$\nabla \cdot \left[f_m (R\epsilon_r \nabla \psi_{1,m} + m\hat{\phi} \times \nabla \psi_{2,m}) \right] + \frac{\epsilon_r \psi_{1,m}}{R} = 0 \tag{5a}$$

$$\nabla \cdot \left[f_m (R\mu_r \nabla \psi_{2,m} - m\hat{\phi} \times \nabla \psi_{1,m}) \right] + \frac{\mu_r \psi_{2,m}}{R} = 0 \tag{5b}$$

where the cross sectional gradient operator is defined by

$$\nabla = \hat{R}\frac{\partial}{\partial R} + \hat{Z}\frac{\partial}{\partial Z} \tag{6a}$$

and

$$f_m = \left[\epsilon_r(R,Z)\mu_r(R,Z)R^2 - m^2 \right]^{-1} \tag{6b}$$

is the media variable which is a determinant of the disjoint first order system. It presents a complication in the form of a singularity at the cylindrical surface defined by

$$R_m(Z) = \frac{|m|}{\sqrt{\epsilon_r(R_m,Z)\mu_r(R_m,Z)}} \tag{7}$$

for the lossless case when the relative parameters, ϵ_r and μ_r, are both real. Numerical errors are observed in the vicinity of these singularities. At points close to such surfaces, and there may be several when layered dielectrics are considered, these errors can be minimized by taking an

averaged value at the point from the CAPs at the surrounding nodes, [25].

Using dyadic operator notation, the system in equation (5) can be rewritten as

$$\overline{\overline{\mathcal{L}}} \cdot \overline{\Psi}(R, Z) = \overline{0} \tag{8}$$

where the dyadic operator, $\overline{\overline{\mathcal{L}}}(R, Z)$, is given by

$$\overline{\overline{\mathcal{L}}} = \begin{bmatrix} \nabla \cdot (f_m R \epsilon_r \nabla) + \epsilon_r / R & m \nabla \cdot (f_m \hat{\phi} \times \nabla) \\ -m \nabla \cdot (f_m \hat{\phi} \times \nabla) & \nabla \cdot (f_m R \mu_r \nabla) + \mu_r / R \end{bmatrix} \tag{9a}$$

and where the column vector is

$$\overline{\Psi}(R, Z) = \begin{bmatrix} \psi_{1,m} \\ \psi_{2,m} \end{bmatrix} \tag{9b}$$

The operator in (9a) can be shown to be self-adjoint where the boundary conditions along the unimoment perimeter are Dirichlet and homogeneous Neumann along the Z-axis. If an appropriate numerical procedure is used, this self-adjointness results in symmetry of the resulting system of linear equations.

2.3 Finite Element Method

The CAP equations require numerical solution within the inhomogeneous regions associated with the scattering problem. The choice of finite elements leads to two equivalent numerical procedures in this case, namely the variational method and the Galerkin method.

The variation statement of the problem is an energy density functional which again can be derived in two ways, one a heuristic method using the system Euler Lagrange equations, the other from a generalized *stationary theorem*.

$$F = \int_S L(R, Z, \psi_1, \psi_2, \nabla\psi_1, \nabla\psi_2)\, dR\, dZ \tag{10}$$

where the modal subscripts have been omitted for clarity and the Lagrangian is given by

$$L = f_m[\nabla\psi_1 \cdot (R\epsilon_r \nabla\psi_1 + m\hat{\phi} \times \nabla\psi_2) + \nabla\psi_2 \cdot (R\mu_r \nabla\psi_2 - m\hat{\phi} \times \nabla\psi_1)] - (\epsilon_r\psi_1^2 + \mu_r\psi_2^2)/R \tag{11}$$

The physical nature of this functional can be shown to be related to the difference between the time-varying and time-average radiated power densities via a *pseudo* (non-conjugate) Poynting vector [24]:

$$F = -\jmath \oint_{\delta S} (\overline{e}_m \times \overline{h}_m) \cdot \hat{n}\, R\, |dc| \tag{12}$$

In (10), S is the finite element cross-sectional area and δS in (12) is the contour which bounds S while c is the length variable around this contour.

The variational method as applied to finite elements begins by using an approximate piecewise polynomial model of the true solution and then a representative approximation at each node of a mesh description of the problem. The problem variables now become the nodal approximates. Since the system is in dynamic equilibrium, the minimum energy condition can be used to derive the equivalent requirement on each nodal variable. Simply, equation (10) is differentiated with respect to these nodal variables and the result set to zero. The fact that the first variation gives a functional which is quadratic in form with respect to these nodal variables results in a system of linear equations. Using the interpolation base chosen, each finite element associated with each node contributes to the resulting linear system of equations.

Alternatively,the weighted residual Galerkin method can be applied to the CAP system of equations given by (8) and (9)

$$\langle W_i, \overline{\overline{\mathcal{L}}} \cdot \overline{\Psi}^*(R,Z) \rangle = \overline{0} \qquad \text{for } i = 1, n_I \tag{13}$$

where n_I is the total number of internal nodes within the finite element mesh, $W_i(R,Z)$ are weighting functions, $\overline{\Psi}^*(R,Z)$ are piecewise polynomial approximations to the exact CAP solution and the $\langle \cdot, \cdot \rangle$ represents an inner-product integration in (R,Z). The * superscript notation employed here and in the next section indicates the numerical approximation to the functional term and does *not* mean complex conjugation. In *Galerkin's* method, the weighting functions and the basis functions for $\overline{\Psi}^*$ are chosen to be equal.

Note that the variational method depends upon discovering the associated quadratic functional, which may or may not exist, whereas the Galerkin approach depends only upon the existence of a unique solution to the system of partial differential equations which depends partially upon the type of boundary conditions being applied. Once these uniqueness constraints are satisfied, Galerkin's method can be applied.

a. Modelling and Shape Functions

Central to the art of numerical modelling is the replacement of the exact solution at all points in the domain of interest with the nodal approximates using a piecewise polynomial representation. It is most essential that the choice of polynomial be representative of the true solution as far as possible given numerical convenience and error considerations. In seeking to obtain the solution of the CAP equations, it must be remembered that the true solution is azimuthally smooth due to the axisymmetry. Hence, the separation of the azimuthal coordinate by the spectral series eqns (2) should be a good approximation for the continuous azimuthal component of the solution. This is not so in all spherical directions, e.g. radial and elevational as inhomogeneities in these directions will cause discontinuities in the cross-sectional fields. For these directions, it is more accurate to use low order piecewise monomial functions $(1, x, x^2, \ldots)$.

In the present study, linear cross-sectional interpolation was employed. This was done in order to utilize the resulting discontinuous numerical solution across media interfaces. This models the exact solution at these boundaries, while also introducing small numerical errors at element interfaces everywhere else. It also allows the use of the Riccati transformation [2] to solve the resulting block-tridiagonal system of linear equations.

For the linear case, a triangular element e is considered. As per equation (9b), let

$$\overline{\Psi}^*_e(R, Z) = [\psi^*_1(R, Z), \psi^*_2(R, Z)]^T_e \tag{14}$$

where T means transpose, represent the approximation to the exact CAP vector by using linear basis functions within the element. As previously mentioned, the * notation indicates numerical approximation and does not mean complex conjugation.

The linear interpolation model is chosen such that it forms a complete polynomial representation of order one within the triangular element.

$$\psi_1^*(R,Z) = a_1 R + a_2 Z + a_3 \tag{15a}$$

$$\psi_2^*(R,Z) = b_1 R + b_2 Z + b_3 \tag{15b}$$

It follows that,

$$\psi_1^*(R,Z) = \underline{P}(R,Z) \cdot \bar{a} \tag{16a}$$

$$\psi_2^*(R,Z) = \underline{P}(R,Z) \cdot \bar{b} \tag{16b}$$

where the row vector is given by $\underline{P}(R,Z) = [R,Z,1]$
and

$$\bar{a} = \begin{Bmatrix} a_1 \\ a_2 \\ a_3 \end{Bmatrix} \qquad \bar{b} = \begin{Bmatrix} b_1 \\ b_2 \\ b_3 \end{Bmatrix}$$

By interpolation, $\bar{\Psi}_e^*(R,Z)$ can be derived in terms of the nodal values of the potentials. These nodal values are represented by the arrays

$$\bar{\psi}_k^e = \begin{bmatrix} \psi_k^*(R_1,Z_1) \\ \psi_k^*(R_2,Z_2) \\ \psi_k^*(R_3,Z_3) \end{bmatrix} \tag{17}$$

where the ordered nodal coordinates of the triangle are (R_n, Z_n) for $n = 1,2,3$, with $k = 1,2$ indicating the two CAP's.

Using the interpolation model at each node of the triangle leads to the fundamental finite element equations

$$\psi_k^*(R,Z) = \underline{N_e}(R,Z) \cdot \bar{\psi}_k^e \tag{18}$$

with $\underline{N_e}(R,Z) = \underline{P}(R,Z) \cdot \bar{\bar{G}}_e$. The transformation matrix is given in terms of the triangle node coordinates

$$\overline{\overline{G}}_e = \begin{bmatrix} R_1 & Z_1 & 1 \\ R_2 & Z_2 & 1 \\ R_3 & Z_3 & 1 \end{bmatrix}^{-1} \tag{19}$$

$$= \frac{1}{2A_e} \begin{bmatrix} (Z_2 - Z_3) & (Z_3 - Z_1) & (Z_1 - Z_2) \\ (R_3 - R_2) & (R_1 - R_3) & (R_2 - R_1) \\ (R_2 Z_3 - R_3 Z_2) & (R_3 Z_1 - R_1 Z_3) & (R_1 Z_2 - R_2 Z_1) \end{bmatrix}$$

where A_e is the area of the triangle.

The shape function vector, $\underline{N_e}(R, Z)$, is composed of three linear function components, $N_n(R, Z)$, each of which equates to unity at the n-th local node and zero at all other nodes in the element. The shape function equations in (18) effectively split the approximate solution into a geometric part and a nodal part. The geometric part is the shape function and depends only on (R, Z). On the other hand, the nodal variable approximates do not depend on the spatial variables directly but rather depend for accuracy on the numerical procedure used to model the underlying partial differential equations. The combined effect is a cross-sectional piecewise planar approximation to the exact wave solution.

The weighted residual Galerkin method can be applied using equations (13), where the weighting functions, W_i, become the components of the shape function vector in each element, resulting in

$$\sum_{e \in \{e(i)\}} \iint_{A_e} \overline{\overline{N}}_i \cdot \{\overline{\overline{\mathcal{L}}} \cdot \overline{\Psi}_e^*(R, Z)\} \, dA_e = \overline{0} \qquad \text{for } i = 1, n_I \tag{20a}$$

where

$$\overline{\overline{N}}_i(R, Z) = \begin{bmatrix} N_i(R, Z) & 0 \\ 0 & N_i(R, Z) \end{bmatrix} \tag{20b}$$

This sum is over the elements connected to the i-th internal mesh node, as is represented by the set $\{e(i)\}$. The dyadic operator, $\overline{\overline{\mathcal{L}}}(R, Z)$, is defined in (9).

Inserting the shape function equations from (18) yields at each node, $n = i, j, k$ within the element $e(i)$,

$$\sum_{e\in\{e(i)\}} \iint_{A_e} \overline{\overline{N}}_i \cdot \overline{\overline{\mathcal{L}}} \cdot \overline{\overline{N}}_n \cdot \begin{bmatrix} \psi_1^i \\ \psi_2^i \end{bmatrix} dA_e = \begin{bmatrix} 0 \\ 0 \end{bmatrix} \tag{21}$$

The divergence theorem is used to reduce the admissibility constraints on the basis functions. This transfers a degree of this constraint to the weighting functions and produces the *weak* form often used in finite element applications [11]

$$\sum_{e\in\{e(i)\}} \iint_{A_e} \overline{\overline{\mathcal{L}}}_N(R,Z) \cdot \begin{bmatrix} \psi_1^i \\ \psi_2^i \end{bmatrix} dA_e = \begin{bmatrix} 0 \\ 0 \end{bmatrix} \tag{22}$$

where $\overline{\overline{\mathcal{L}}}_N(R,Z)$ is given by

$$\begin{bmatrix} f_m \nabla N_i \cdot (R\epsilon_r \nabla N_n) - N_i N_n \epsilon_r / R & m\nabla N_i \cdot (f_m \hat{\phi} \times \nabla N_n) \\ -m\nabla N_i \cdot (f_m \hat{\phi} \times \nabla N_n) & f_m \nabla N_i \cdot (R\mu_r \nabla N_n) - N_i N_n \mu_r / R \end{bmatrix}$$

As stated, the variational method results in an equivalent system of equations to that generated by the coupled differential equations.

b. Conformal Mesh

The techniques used to define the placement of the finite elements throughout the domain of the inhomogeneous problem within the separable surfaces relate to both the linear equation solution method and the type of spatial problem being analyzed. As well, the degree of inhomogeneity and the presence of discontinuities of either media or geometry all affect the mesh generation process.

For near spherical geometries, the use of a double semi-circular boundary allows a constant radial width. Thus, a domain may be modelled by distorting what is essentially a regular polar coordinate mesh to conform to the dielectric-air interface (and additionally the conductor-dielectric interface for composite bodies).

The placement of nodes along each radial is performed in the manner discussed by Morgan [24] such that a regular polar mesh is minimally perturbed. The dielectric (and conductor) surface of revolution can be defined by an radius array $R_i = R(\theta_i)$, for $i = 1, I_{max}$. The

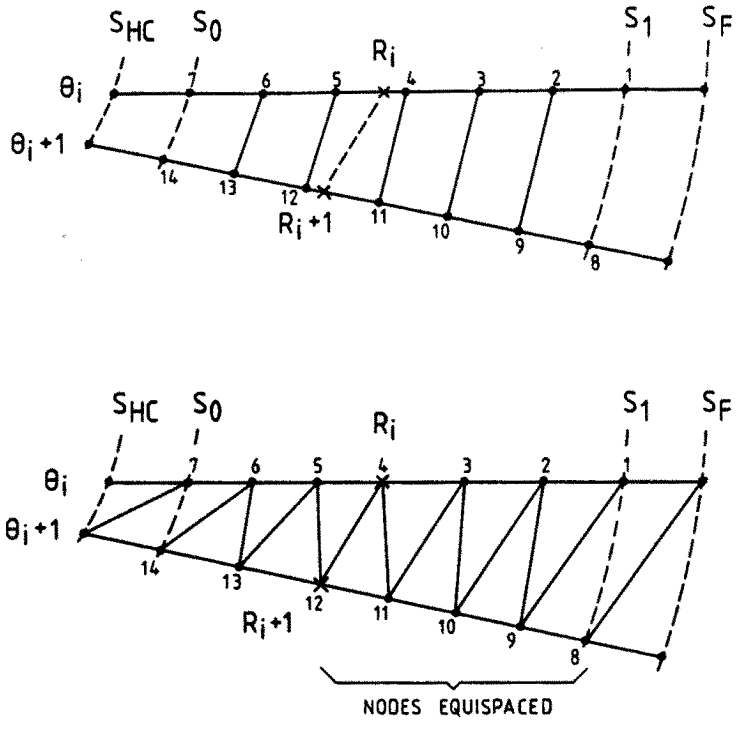

Figure 4 Conformal mesh generation for 3-node triangles.

object is to choose the node in the original undisturbed mesh that is closest to the surface R_i at each θ_i as shown in Fig. 4.

The same procedure can be generalized for multi-layered problems such as the tip effects of a multi-layered radome [22] and the analysis of *hot-spots* within the human cranium [8].

The convenience of the mesh is increased by keeping the number of nodes along each radial spoke constant. The topology is equivalent at each step starting from $\theta = 0°$ to $\theta = 180°$. Figure 5 illustrates the mesh for an off-set loaded conducting sphere where the global node numbering is shown for the first three radial steps. The grid can be adapted for regions of greater change, for example, the bicone shape near the half-angle.

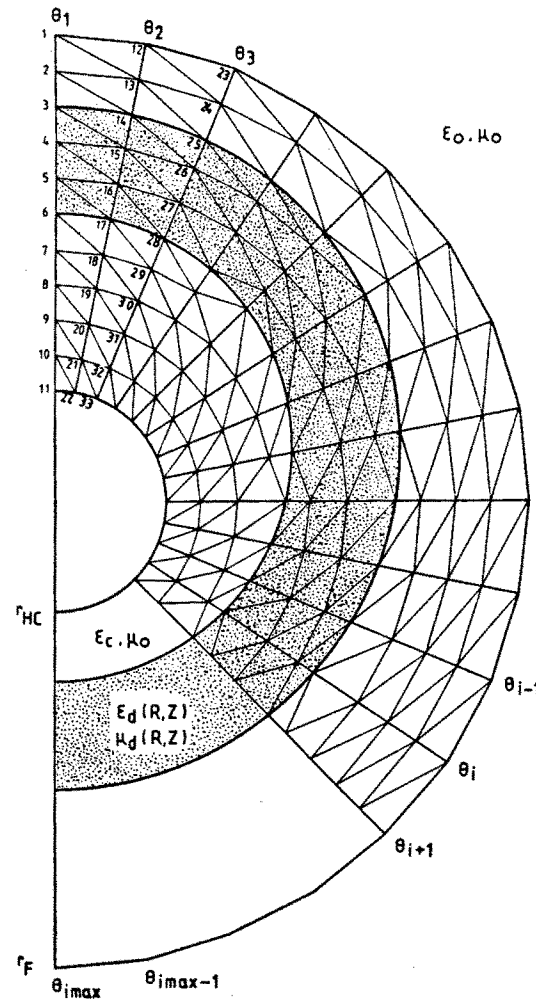

Figure 5 Mesh for offset loaded conducting sphere.

c. *Riccati Transform*

As was previously described, the system matrix is gradually loaded as the forward sweep continues until the last radial is reached. The resulting matrix is shown diagrammatically in Fig. 6. It can be seen that the structure is tridiagonal in sub-matrices formed by the partition into the nodal unknowns associated with each radial unknowns vector, $\overline{\Psi}_i$.

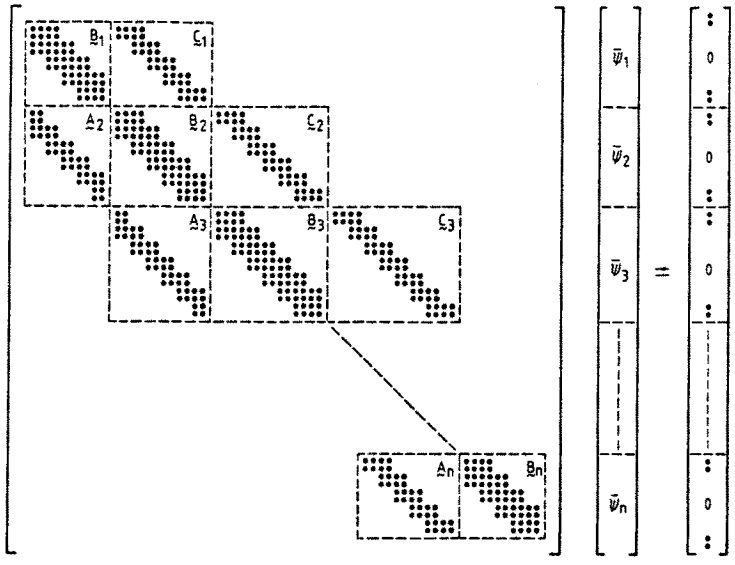

Figure 6 Single mode global system matrix.

The off-diagonal sub-matrices reflect the RH or LH nature of the local mesh distortions and are banded of half-width 3, whilst the main diagonal has a half-width of 4. Each submatrix can be stored in a banded profile fashion whereby only the band coefficients and the column number of the left-most entry of the band in each row is required.

The Riccati block-by-block elimination technique [2] can be used to solve the system of linear equations. The system matrix may be written in terms of a recursive sequence of submatrices.

$$\overline{\overline{A}}_i \cdot \overline{\Psi}_{i-1} + \overline{\overline{B}}_i \cdot \overline{\Psi}_i + \overline{\overline{C}}_i \cdot \overline{\Psi}_{i+1} = \overline{D}_i \qquad \text{for } i = 1, 2, \ldots I_{max} \quad (23)$$

where, by inspection, the initial and final submatrices

$$\overline{\overline{A}}_1 = \overline{\overline{C}}_1 = \overline{\overline{A}}_{I_{max}} = \overline{\overline{C}}_{I_{max}} = \overline{\overline{0}}$$

In all subsequent computations, the dimensions of the submatrices were kept constant because the nodal grid was so chosen. However, applications where this is not the case can be solved in the same fashion.

If the lengths of $\overline{\Psi}_{i-1}, \overline{\Psi}_i$, and $\overline{\Psi}_{i+1}$ are n_{i-1}, n_i, and n_{i+1}, respectively, then $\overline{\overline{A}}_i, \overline{\overline{B}}_i$ and $\overline{\overline{C}}_i$ have the dimensions $n_i \times n_{i-1}, n_i \times n_i$ and $n_i \times n_{i+1}$; the total dimension of the system matrix will be $\sum_{i=1}^{N} n_i$.

The Riccati matrix, $\overline{\overline{R}}_i$, and vector $\overline{S}_i$ are defined by the transformation

$$\overline{\Psi}_{i-1} = \overline{\overline{R}}_i \cdot \overline{\Psi}_i + \overline{S}_i \tag{24}$$

Substituting (24) into (23) and comparing with the form in (24) gives the following recursive relationships

$$\overline{\overline{R}}_{i+1} = -(\overline{\overline{B}}_i + \overline{\overline{A}}_i \cdot \overline{\overline{R}}_i)^{-1} \cdot \overline{\overline{C}}_i \tag{25a}$$

$$\overline{S}_{i+1} = -(\overline{\overline{B}}_i + \overline{\overline{A}}_i \cdot \overline{\overline{R}}_i) \cdot (\overline{D}_i - \overline{\overline{A}}_i \cdot \overline{S}_i) \tag{25b}$$

The boundary conditions yield the start and end matrix and vector at both ends

$$\overline{\overline{R}}_2 = \overline{\overline{B}}_1^{-1} \cdot \overline{\overline{C}}_1 \tag{26a}$$

$$\overline{S}_2 = \overline{\overline{B}}_1^{-1} \cdot \overline{D}_1 \tag{26b}$$

$$\overline{\overline{R}}_{(I_{max}+1)} = \overline{\overline{0}} \tag{26c}$$

$$\overline{S}_{(I_{max}+1)} = \overline{D}_{(I_{max})} \tag{26d}$$

It can be seen from Fig. 6 that $\overline{\Psi}_i$ has only two non-zero elements at θ_i (apart from the conditions on the z-axis at θ_0 and $\theta_{I_{max}}$). This allows a reduction in core storage requirements although a simple alternative technique is to use backing disk to store and retrieve $\overline{\overline{R}}_i$ and $\overline{S}_i$ as required.

Thus the, linear solution method starts by stepping forward a radial at a time beginning from $\theta = 0°$ to $\theta = 180°$ where at each step the recursive transform equations are used to successively eliminate the previous i-2th radial unknowns vector. The first and last radials lie on the Z-axis and, depending upon the mode being considered and on the CAP variables being used, these conditions are trivially loaded. Once

the final radial at $\theta = 180°$ is reached, the forward evolution is complete and a back substitution stage is now commenced. The solution along each radial is obtained in turn as the backsweep proceeds. If necessary, these solutions can be found for all nodes in each vector; only the congruential nodes were required however for the present application.

d. Incorporation of Conductor Regions

Three methods may be used to incorporate the conducting region:

(a) Perfect conductor boundary conditions may be applied along the cross-sectional contour of the axisymmetric conductor/dielectric interface

$$\psi_{1,m} = 0 \tag{27a}$$

$$\frac{\partial \psi_{2,m}}{\partial n} = 0 \tag{27b}$$

(b) A complex permittivity may be used inside the conductor region where the conductivity of the medium is included; the finite element mesh finishes at an internal separable surface where internal core modes are applied within the unimoment method

$$\epsilon_r = \epsilon_r' - j\epsilon_r'' \tag{28a}$$

where

$$\epsilon_r'' = \sigma/\omega\epsilon_0 \tag{28b}$$

The use of a complex permittivity results from a reformulation of the underlying time-varying wave equations where a first order partial time derivative exists. This derivative can be incorporated within the same time-harmonic formulation as in equations (1) and (5) by redefining a complex propagation constant which can be related to the free-space wave number. Thus $k = k_r k_0$, where the normalization factor is $k_r = \sqrt{\epsilon_r' - j\sigma/\omega\epsilon}$, [26]. In general, the time-varying fields can be shown to be elliptic in direction at any point. The path of a free electron in such a field will also be elliptic; the concept of an eddy current is apparent.

Method (b) is illustrated by Fig. 5. An unreduced nodal separation or mesh step is shown in the conductor region (the mesh is stepped

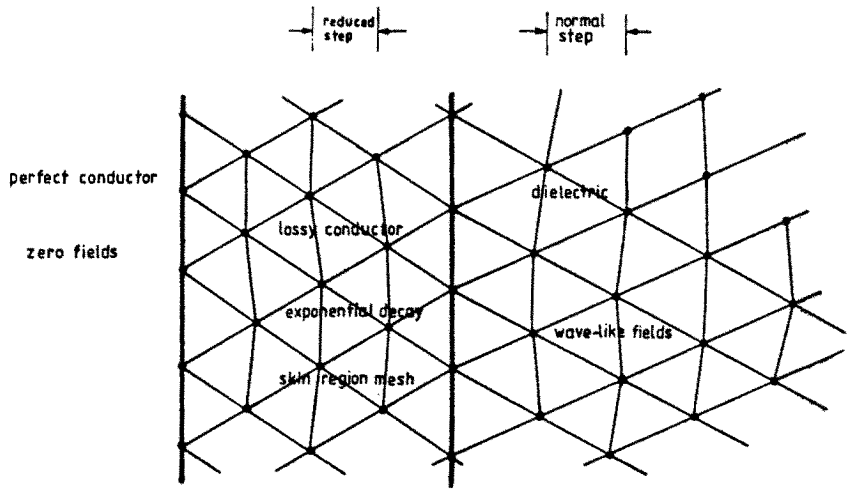

Figure 7 Conductor surface skin model.

inwards from the free-space separable surface at r_F, until the homogeneous core region separable surface at r_{HC} is reached). A range of *poor* conductors may be modelled in this fashion.

(c) An imperfect *skin* region can be modelled by utilizing the same complex permittivity concept as in (b) but terminating the mesh stepping at a boundary just inside the conductor surface; internal to this thin layer, the fields are presumed to have vanished but within the skin they are accounted for. In this case, the position of the internal boundary is varied depending upon precisely where the conductor surface is situated for a particular angle. It is not important precisely where the internal boundary is located, rather that the field gradients near the surface should be accounted for correctly and that the resulting submatrices be kept of nearly constant dimension. The unimoment method is simplified since no internal core modes are required. Within the skin, a reduced nodal separation can be used for modelling actual conductors such as aluminium. Figure 7 illustrates the concept of reducing the step at the surface.

Having previously tried methods (a) and (b), [27], (c) was chosen for numerical testing. The first objects selected for examination were spheres since the analytical Mie series solution was available for com-

parison for both unloaded and loaded spheres and for the additional case of an axial offset with respect to the Z-axis.

The initial problem was to determine what actual nodal step reductions should be used inside the conductor and with what range of ϵ_r''. Using two unloaded centred conducting sphere scatterers (radii $0.4\lambda_0$ and $0.8\lambda_0$), a broad range of step reductions and permittivities was tested to see what relationship would give valid results.

In both cases at each point, the problem parameters were varied such that two or so steps of an iterative multi-dimensional hill search were performed where at the top of the hill lay the optimized approximation to the exact solution. The parameters referred to are I_{max} the number of angular θ divisions, N_{max} the number of radial modes, DENS the nodal mesh density in nodes per wavelength and M_{max} the number of azimuthal modes (only the $m = 1$ mode is required for axial incidence).

Figures 8 and 9 show how ϵ_r'' relates to the step ratio and the forward scattering cross section solution for both sphere problems assuming axial incidence. It is seen in both that the simulation has a stable region between two unstable bounding regions which together demonstrate the quadratic nature of the conductor surface modelling error. The results indicate that there is a broad range of ϵ'' and step ratios within which the numerical errors due to the surface skin model are minimal. Further, as the spherical radius of any point increases, so does the stable region; unfortunately so do the computational requirements.

To further check the procedure, the complex scattering amplitudes for the $0.4\lambda_0$ unloaded sphere and an off-set loaded conducting sphere problem of radius $1.0\lambda_0$ were examined. These results afforded much insight into both amplitude and phase solutions for the finite element program, EMSCAT, which was based on that used by Morgan [24]. These results are shown in Figs. 10 and 11.

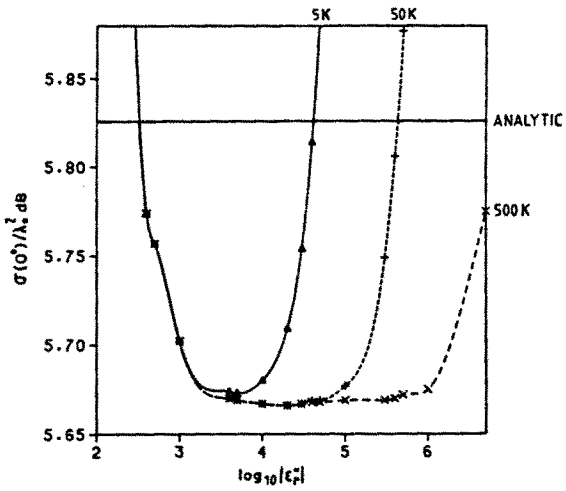

Figure 8 Forward scattering vs. ϵ_r'' within the skin of a $0.4\lambda_0$ radius conducting sphere for various mesh step reductions.

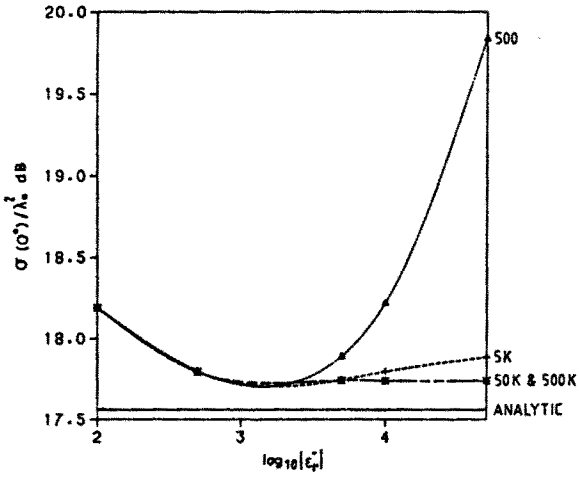

Figure 9 Forward scattering vs. ϵ_r'' within the skin of a $0.8\lambda_0$ radius conducting sphere for various mesh step reductions.

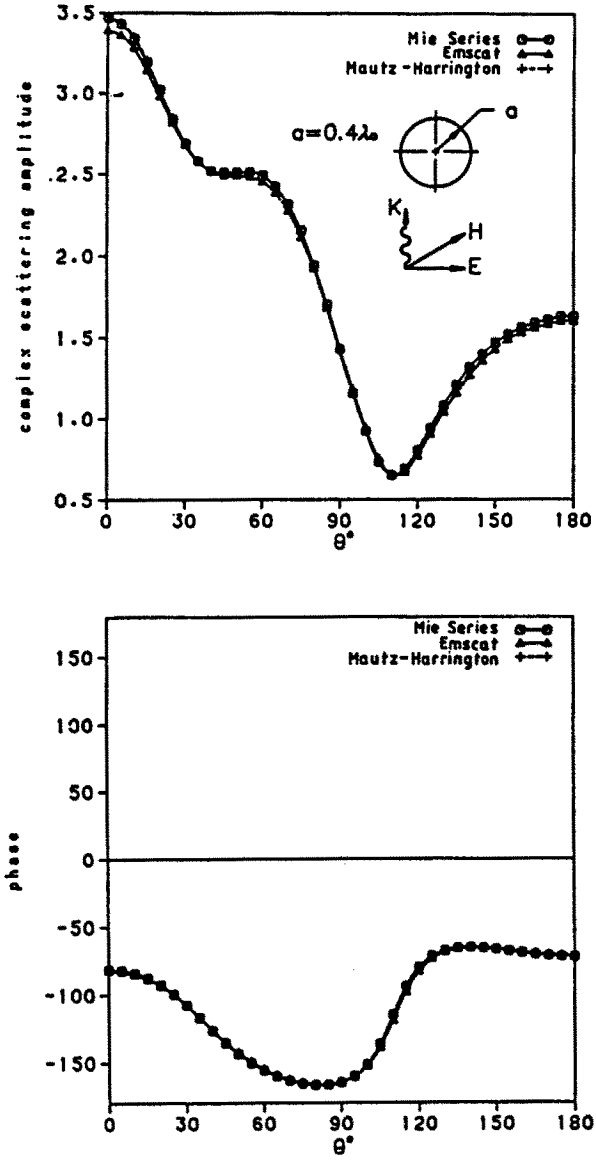

Figure 10 Complex scattering amplitude (magnitude and phase) for $0.4\lambda_0$ unloaded conducting sphere; E-plane pattern with TM incidence.

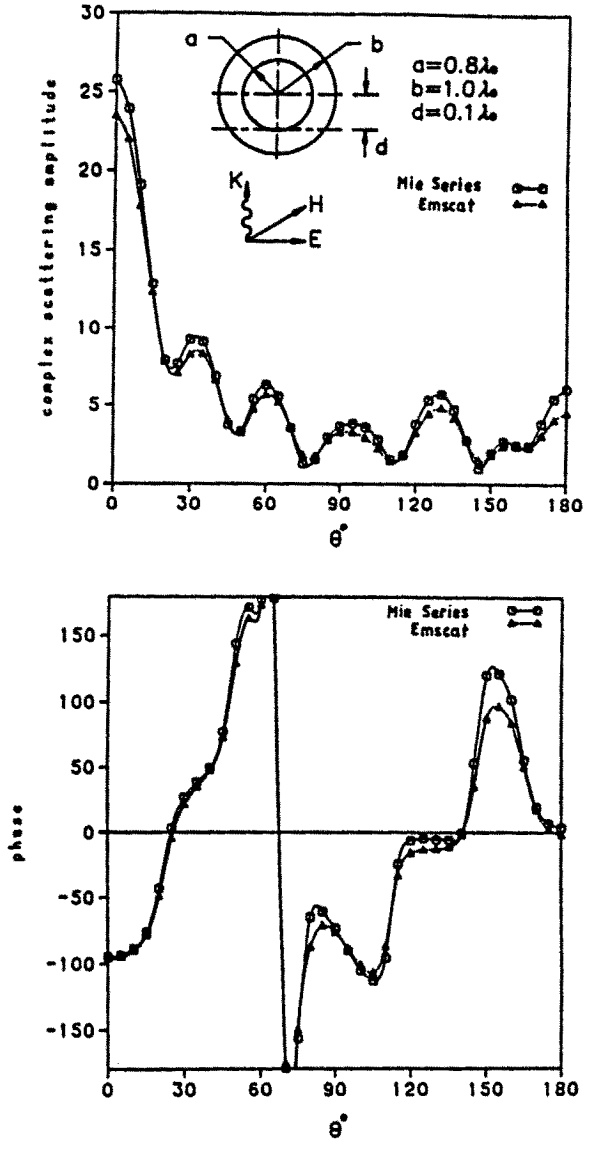

Figure 11 Complex scattering amplitude (magnitude and phase) for loaded offset conducting sphere: a=0.8λ_0, b=1.0λ_0, offset=0.1λ_0, ϵ_r= 2.60; *E*-plane pattern with TM incidence.

2.4 Numerical and Experimental Results

Having obtained a basic confidence in the procedure, a second phase of testing was carried out using more arbitrary shapes involving a wide range of radial distances and sharp corners which might better check the skin model. As a means of comparison, a moment method program based on the SIE approach was used [12]. Other results in the form of monostatic and bistatic radar cross sections were also available [1,4].

Figure 12 shows the bistatic results for a loaded ellipsoid, with $a_1 = 0.3\lambda_0, a_2 = 0.5\lambda_0, b_1 = 0.2\lambda_0, b_2 = 0.3\lambda_0$, and $\epsilon_r' = 4.0$. Figure 13 shows the back scattering cross section for an unloaded sphere-cone of base diameter $0.592\lambda_0$ and half angle 40°. Again the results were reasonably good.

An empirical experiment was also conducted by constructing a range of loaded bicones and accurately measuring the far field scattering. The measurements were carried out at the antenna scattering range at the Defence Research Centre Salisbury (DRCS) in Adelaide, South Australia. Figure 14 shows the monocone pair (a) that screwed together with the various loadings (b)-(f). Monostatic radar cross sections were measured using two polarizations of plane wave (E and H vertical). The measurements were performed at two related frequencies, 9.33 GHz and 4.67 GHz.

Next, the biconical scatterers were numerically analyzed. Up to this point, the cross sectional shapes involved were relatively straight forward to program. With the necessity to model the constructed unloaded and loaded bicones, a more systematic approach was required. The solution was to incorporate a multi-layered capability together with a means of segmenting each contour into elemental shapes, such as sphere, bicone, cylinder etc., each of which was specified within an angular range. This facility, together with a method of varying the permittivity within each layer as the angular evolution is performed, enabled the structures to be modelled.

The back-scattering radar cross sections for the unloaded and loaded bicones, (a) through (f) of Fig. 14, are shown in Figs. 15 to 20. These results were obtained at a frequency of 9.33 GHz. The numerical parameters used were: for the unloaded bicone, $I_{max} = 151$, $N_{max} = 10$, $M_{max} = 7$ (m = 0,1,2...7), DENS = 31 and for the loaded bicones, $I_{max} = 131$, $N_{max} = 14$, $M_{max} = 7$, DENS = 31. Inside the skin region, in all cases, $\epsilon_r'' = 500,000$ and the step reduction ratio was

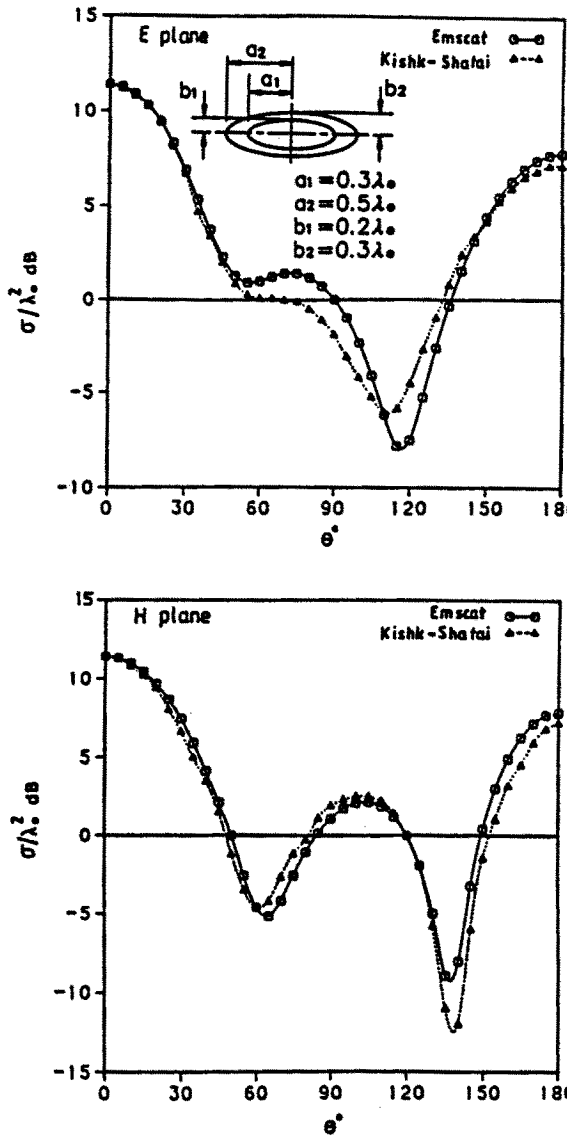

Figure 12 Bistatic radar cross section for a loaded ellipsoid: $a_1=0.3\lambda_0$, $a_2=0.5\lambda_0$, $b_1=0.2\lambda_0$, $b_2=0.3\lambda_0$, $\epsilon_r' = 4.0$; E- and H-plane patterns.

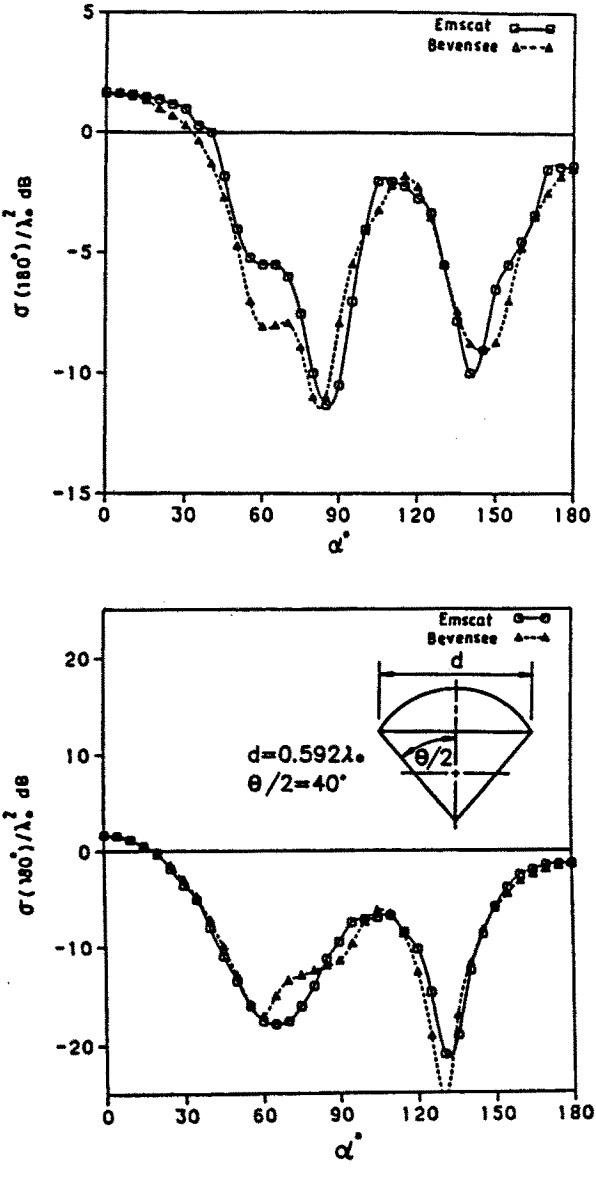

Figure 13 Back scattered radar cross section for an unloaded sphere-cone: base diameter=$0.592\lambda_0$, half-angle=40°; E- and H-plane patterns.

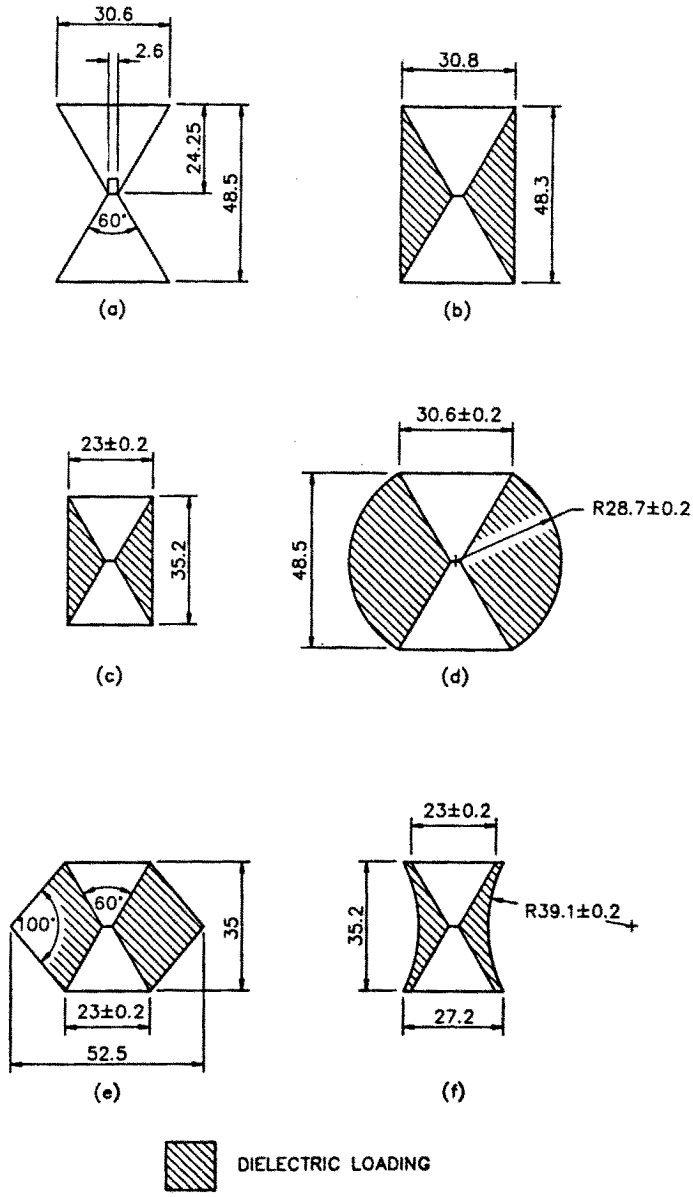

Figure 14 Constructed bicone and loadings: (a) Unloaded bicone; (b) - (f) Various dielectric loadings.

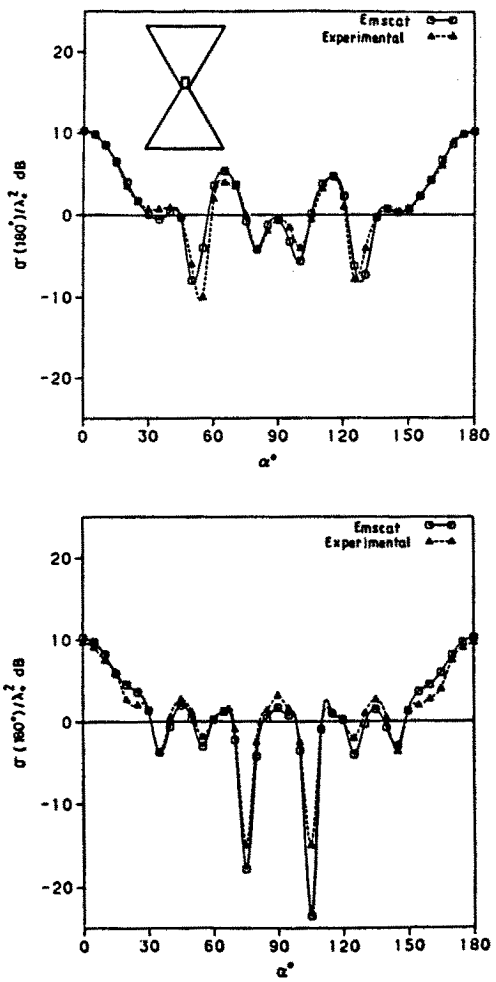

Figure 15 Back scattered radar cross section for the unloaded bicone in Fig. 14(a); (Upper) E-plane and (Lower) H-plane.

5000. The loading dielectric constant, ϵ_r' was measured to be 2.48. The cross section results for the range $0° - 180°$ were obtained by taking 37 individual problems, $\alpha = 0°, 5°, 10° \ldots 180°$, utilizing the economy of effort of the unimoment method. The errors for bicones (a),(b),(c) and (f) can be seen to be reasonable ($\pm 2dB$) where the experimental and

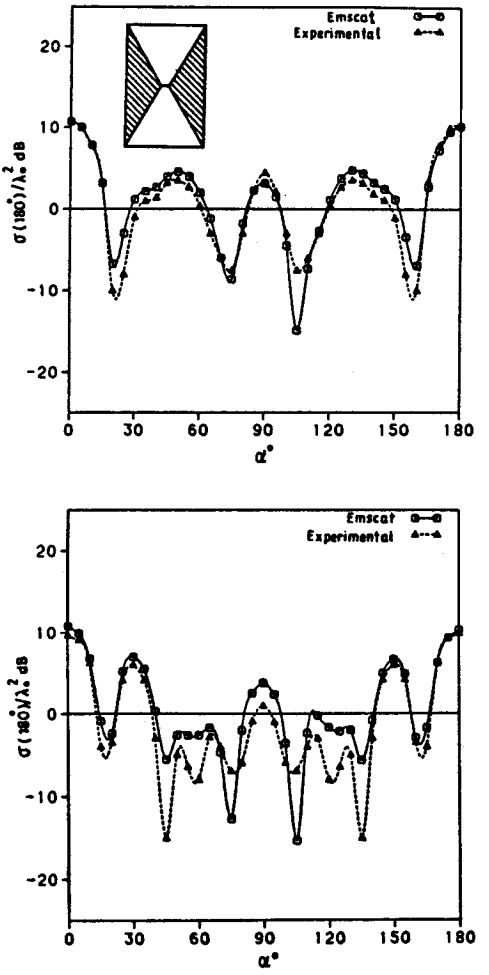

Figure 16 Back scattered radar cross section for the loaded bicone in Fig. 14(b); (Upper) E-plane and (Lower) H-plane.

numerical levels were above their respective noise floors. Loadings in bicones (d) and (e) protrude sufficiently to transverse the cylindrical singularity at $0.64\lambda_0$. The results for bicone (d) indicate the deterioration expected in the range $\theta = 46° - 134°$, while those for bicone (e) confirm that any effect is localized to a smaller range near broadside.

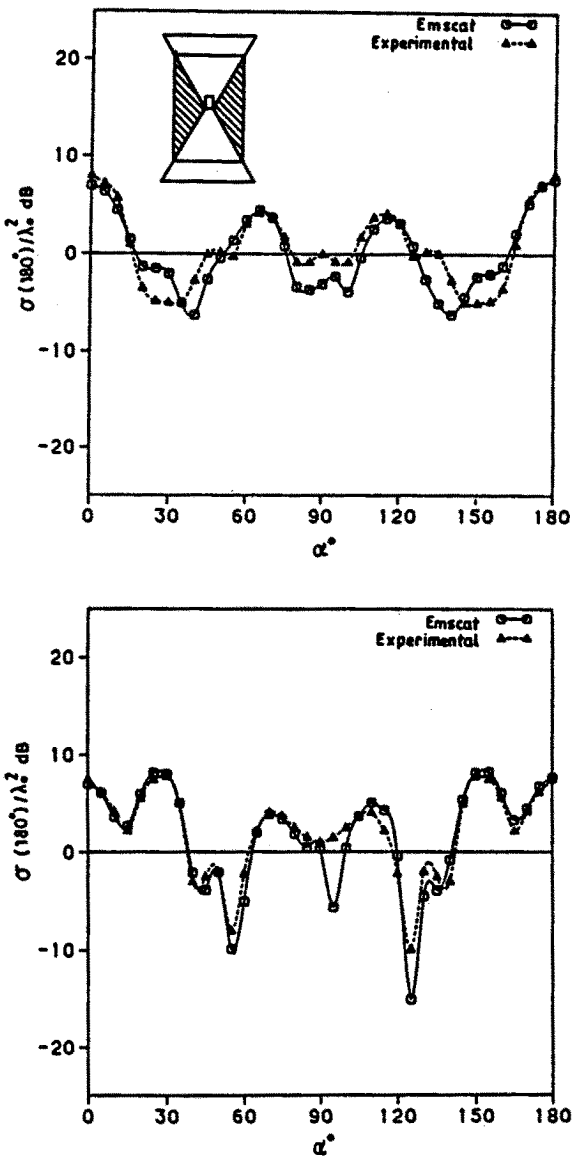

Figure 17 Back scattered radar cross section for the loaded bicone in Fig. 14(c); (Upper) *E*-plane and (Lower) *H*-plane.

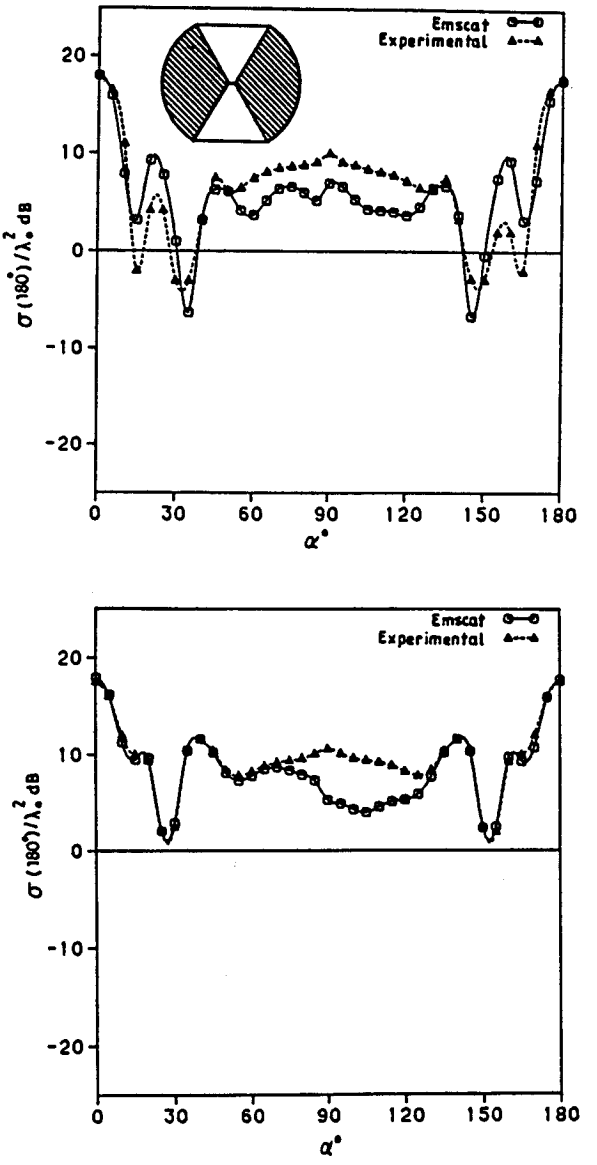

Figure 18 Back scattered radar cross section for the loaded bicone in Fig. 14(d); (Upper) E-plane and (Lower) H-plane.

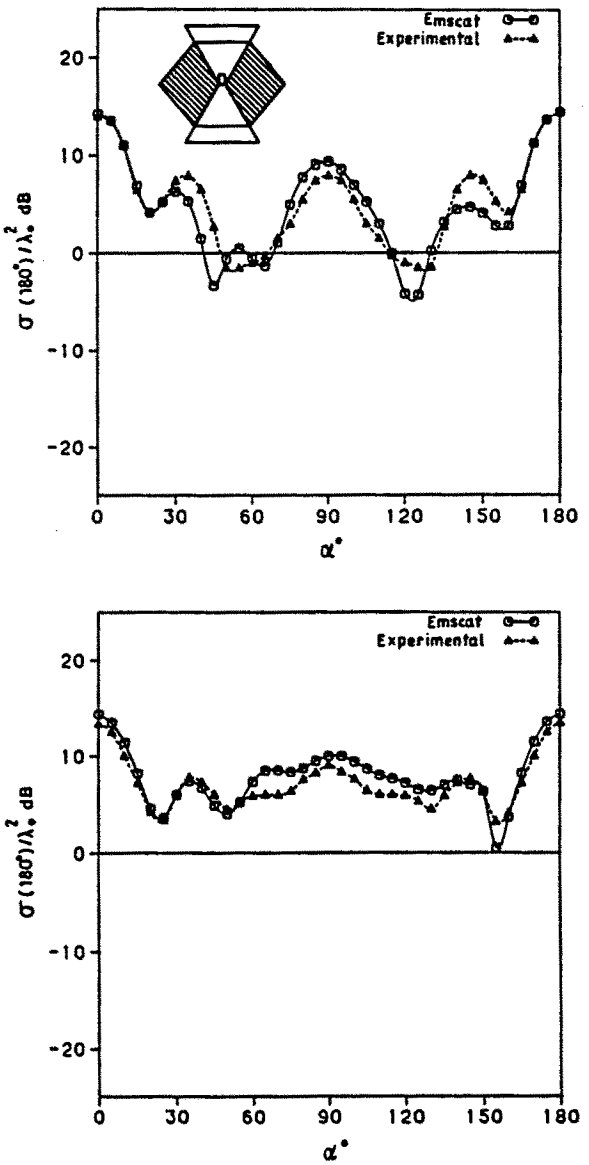

Figure 19 Back scattered radar cross section for the loaded bicone in Fig. 14(e); (Upper) *E*-plane and (Lower) *H*-plane.

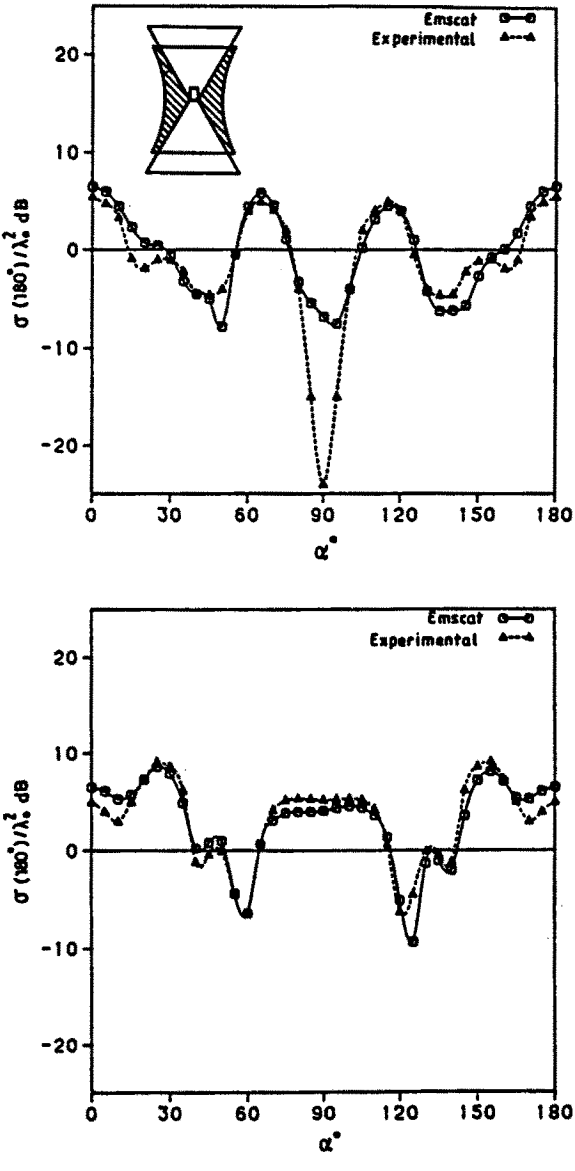

Figure 20 Back scattered radar cross section for the loaded bicone in Fig. 14(f); (Upper) *E*-plane and (Lower) *H*-plane.

2.5 Conclusions

The results of the experimental and numerical testing demonstrate inclusion of conductor surfaces within the CAP/unimoment algorithm. The method most successfully applied was the modelling of a thin surface skin region similar to the actual situation at a real conductor surface.

The selection of ϵ_r'' requires careful consideration. Those parts of the structure near the origin necessitate a higher skin permittivity to ensure accurate modelling which leads to extra computing resources such as dynamic range.

The model also requires the overheads associated with the extra nodes of the skin region. By using perfect boundary conditions, such overheads could be avoided at the cost of accuracy. Fortunately, these extra nodes are minimal since the solution form inside the skin is exponentially decaying and linear interpolation can accurately model the decay near the surface at relatively little cost. Throughout the computations, the core region unimoment method was not required which was achieved by setting the internal number of modes to zero. Thus, three extra nodes were included in the mesh beyond the conductor-dielectric interface. The test results of centred unloaded and loaded spheres indicate that accurate results can be obtained in this fashion.

The types of composite objects analyzed in Sections 2.3 and 2.4 were special cases in the sense that in each, the conductor formed the internal core region. Consider the case of a surgically implanted metallic plate which acts as a replacement for the bone covering the brain. In this case, the composite structure is not so straightforward and the conductor does not preclude the internal region if the origin is placed at the brain centre [8]. Structures such as this may be analyzed by inserting two skin regions on each side of the plate as the θ evolution proceeds. By once again ensuring that the number of nodes along each radial is kept fairly constant, the same solution procedure can be used.

2.6 Future Developments

All bodies of revolution may be called azimuthally homogeneous. Other more spatially arbitrary objects can be classified as:

- azimuthally piecewise homogeneous
- azimuthally continuously inhomogeneous with *slow* variations
- azimuthally continuously inhomogeneous with abrupt variations

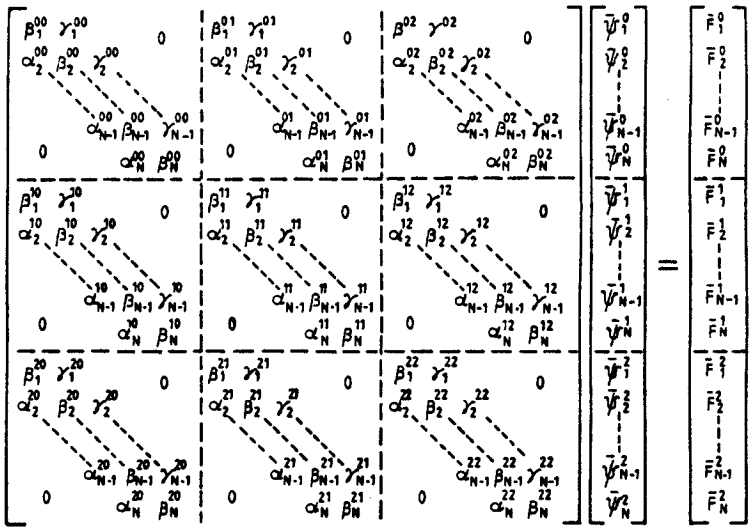

Figure 21 Global system matrix for quasi-axisymmetric case.

Thus, a range of geometries exist that lie between axisymmetric and arbitrarily 3-dimensional objects which can be called piecewise axisymmetric or quasi-axisymmetric.

Material objects whose constitutive properties vary around the azimuth form important modern problems. The human body might be approximated in a piecewise axisymmetric fashion. Nebular gases such as plume exhaust form an example of *slow* axial inhomogeneity. Likewise, there are structures that exhibit abrupt azimuthal discontinuities such as a half-sphere which is aligned with its equator along the Z-axis.

Many of the concepts behind the axisymmetric CAP/unimoment method are capable of being generalized to allow the solution of these more arbitrary electromagnetic problems (*Editor's Note:* See Chapter 6). Quasi-axisymmetric objects may be analyzed by using a fully coupled version of the CAP equations [23]. In addition to the spectral series for the fields, a second series for azimuthal variations in the constitutive parameters $\epsilon(\rho,\theta,\phi)$ and $\mu(\rho,\theta,\phi)$ can be used. Maxwell's equations no longer decouple or reduce at each mode and all 6 modal variables are required. However the resulting system, illustrated in Fig. 21 has a Toeplitz-like replication and importantly the unimoment

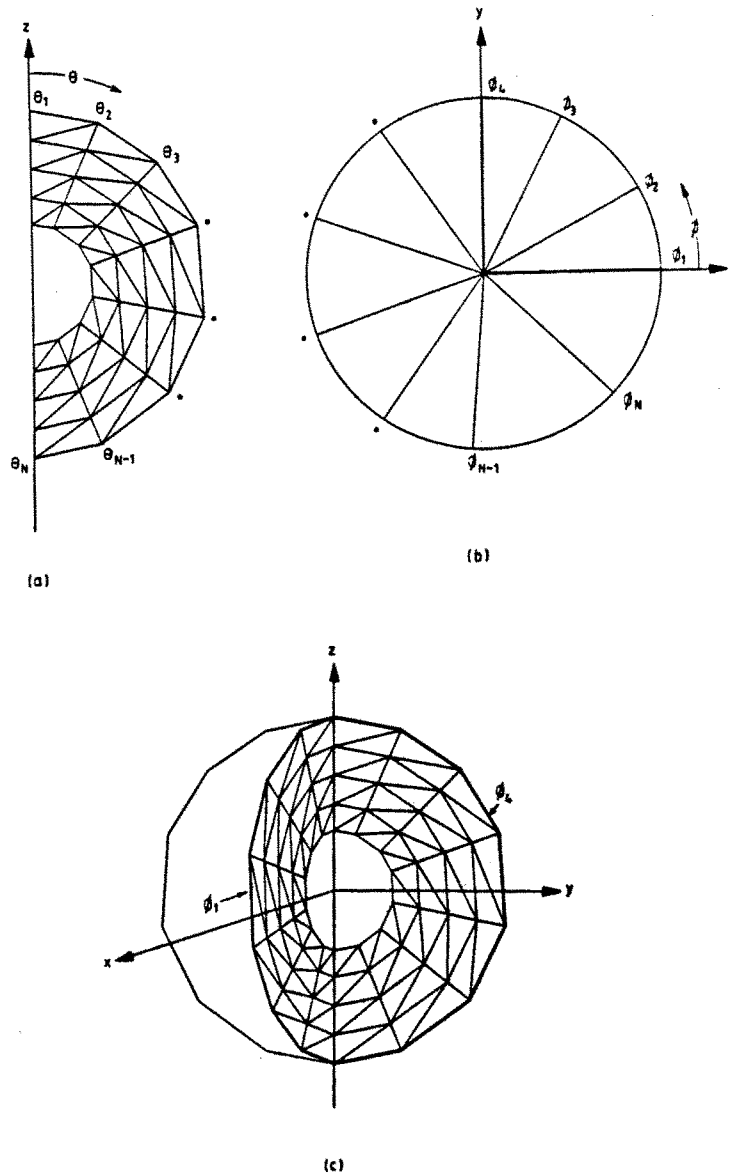

Figure 22 Azimuthally segmented mesh for the piecewise axisymmetric case: (a) Meridian section, (b) Azimuthal segments, (c) Open view of 3-D mesh structure.

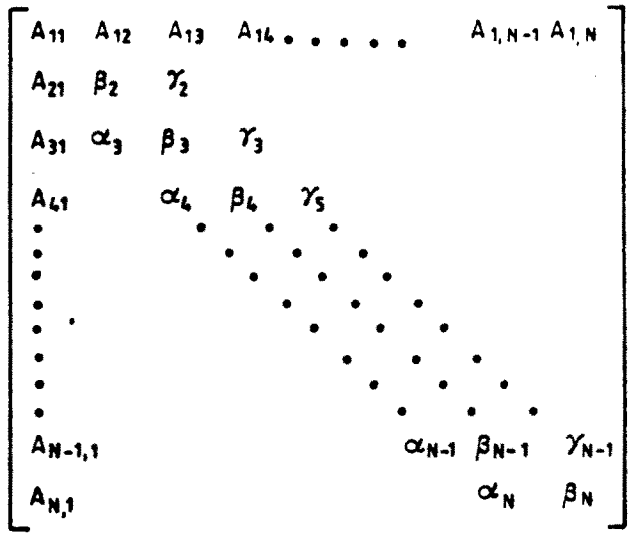

Figure 23 Global system matrix for piecewise axisymmetric case.

method can be applied to ensure continuity of the fields at the freespace separable contour. Although the submatrices are sparse, the overall matrix is dense and is now $3m$ times the size of the axisymmetric matrix, where m is the number of azimuthal modes required.

Continuous spectral functions are most appropriate in the axisymmetric and quasi-axisymmetric cases where the fields are azimuthally smooth. Other bases can be used for problems involving azimuthal discontinuities. Spectral functions, periodic in higher multiples of 2π such as 4π etc., or non-periodic bases including monomial functions may be used to account for jump discontinuities [28]. Piecewise spectral functions result in a piecewise axisymmetric formulation where the axisymmetric CAPs may be used within an azimuthal segment.

The axisymmetric conformal mesh generation procedure illustrated in Fig. 5 can be projected around the azimuth to sectionally conform to a three dimensional contour of arbitrary shape. As with the axisymmetric mesh, multi-layered objects or continuously inhomogeneous objects can be mapped. Figure 22 shows an azimuthally segmented mesh while the resulting submatrix structure is shown in Fig. 23. The topology is interesting in that a star connection forms along the Z-axis. A

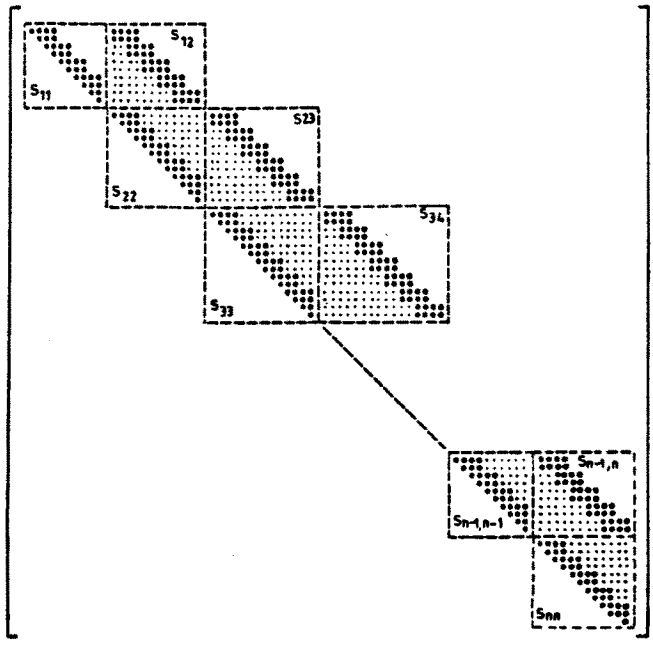

Figure 24 Sparse LU-decomposition of a block tridiagonal matrix.

simpler submatrix can be achieved where the region along the Z-axis is axisymmetric; here the unimoment method can be used to account for the possibly layered core regions.

Direct methods for solving large sparse systems of equations often suffer from complete fill-in of the submatrices. The Riccati transformation, as employed in Section 2.3 c., is one such method. Sparse factorization can avoid unnecessary computations resulting from fill-in. Recently, direct and iterative sparse factorization methods have been reported where the filled-in terms decay rapidly and may be ignored upon reaching some predetermined residual measure [29]. Such schemes would appear to be well suited to the present application and to the above suggestions for analyzing non-axisymmetric problems. Figure 24 illustrates Choleski LU factorization as applied to block-tridiagonal systems. The work factor using complete submatrix inversion is $O(n^3)$, where n is the dimension of a particular submatrix; it can be shown that this is reduced to order $O(r^2 n)$ where r is a reduced bandwidth resulting from ignoring the residual fill-in terms.

Acknowledgements

The author would like to thank the management and staff of the Department of Defence, both at Victoria Barracks in Melbourne and at Salisbury in Adelaide, for their support and assistance. He also wishes to thank Prof. Michael Morgan (The Naval Postgraduate School, Monterey, CA) for his detailed communications. A debt of thanks is due to the author's supervisors, Dr. Don Sinnott (Defence Research Centre Salisbury, South Aust.) and Dr. Ken Mann (Chisholm Institute of Technology, Caulfield, Victoria). Dr. Stan Davies (Telecom Research Laboratories, Clayton) kindly assisted in the preparation of this document.

References

[1] Bevensee, R. M., *A Handbook of Conical Antennas and Scatterers*, Gordon and Breach Science Publishers, 1975.

[2] Stovall, R. E., and K. K. Mei, "Application of a unimoment technique to a biconical antenna with inhomogeneous loading", *IEEE Trans. Antennas Propagat.*, **AP-23**, 335–341, 1975.

[3] Govind, S., D. R. Wilton, and A. W. Glisson, "Scattering from inhomogeneous penetrable bodies of revolution," *IEEE Trans. on Antennas and Propagat.*, **AP-32**, 1163–1173, 1984.

[4] Kishk, A. A., and L. Shafai, "Numerical solution of scattering from coated bodies of revolution using different integral equation formulations", *IEE Proceedings*, **133**, Pt. H, No. 3, 1986.

[5] Joyner, A. H., B. Hocking, A. H. J. Fleming, and I. P. Macfarlane, "Metallic implants and exposure to RF radiation," *Radiation Protection Practice: Proc. IRPA 7th Int. Congress*, **1**, 477-484, 1988.

[6] Mei, K. K., "Unimoment method of solving antenna and scattering problems," *IEEE Trans. Antennas Propagat.*, **AP-22**, 760–766, 1974.

[7] Morgan, M. A., S. K. Chang, and K. K. Mei, "Coupled azimuthal potentials for electromagnetic field problems in axially symmetric media," *IEEE Trans. Antennas Propagat.*, **AP-25**, 413–417, 1977.

[8] Morgan, M. A., "Finite element computation of microwave absorption by the cranial structure," *IEEE Trans. Biomedical Eng.*, **BME-28**, 687–696, 1981.

[9] Durney, C. H., "EM dosimetry for models of humans and animals: a review of theoretical and numerical techniques," *Proc. IEEE*, **68**, 33–40, 1980.

[10] Moilel, R. A., S. K. Wolfson, Jr., R. G. Selker, and S. B. Weiner, "Materials for selective tissue heating in a radiofrequency EM field for the combined chemothermal treatment of brain tumors," *J. Biomed. Mater. Res.*, **10**, 327–334, 1976.

[11] Brebbia, C. A., "The boundary element method," Short Course Notes, Chisholm Institute of Technology, August 23–25, 1983.

[12] Mautz, J. R., and R. F. Harrington, "H-field, E-field and combined field solutions for conducting bodies of revolution," *AEU*, **32**, 157–164, 1978.

[13] Wu, T. K., and L. L. Tsai, "Scattering from arbitrarily-shaped lossy dielectric bodies of revolution," *Radio Science*, **12**, 709–718, 1977.

[14] Harrington, R. F., *Field Computation by Moment Methods*, New York: MacMillan, 1968.

[15] Hagmann, M. J., O. P. Gandhi, J. D'Andrea, and I. Chaterjee, "Head resonance: numerical solutions and experimental results," *IEEE Trans. Microwave Theory Tech.*, **MTT-27**, 809–813, 1979.

[16] Lynn, P. P., and H. A. Hadid, "Infinite elements with $1/r$ type decay," *Int. Journal for Numerical Methods in Engineering*, **17**, 347–355, 1981.

[17] Chiang, K. S., "Finite element method for cutoff frequencies of weakly guiding fibres of arbitrary cross-section," *Optical and Quantum Electronics*, **16**, 487–493, 1984.

[18] Morgan, M. A., and B. E. Welch, "The field feedback formulation for electromagnetic scattering computations," *IEEE Trans. on Antennas and Propagat.*, **AP-34**, 1377–1382, 1986.

[19] Morgan, M. A., and K. K. Mei, "Finite element computation of scattering by inhomogeneous bodies of revolution," *IEEE Trans. Antennas Propagat.*, **AP-27**, 203–214, 1979.

[20] Morgan, M. A., "Finite element computation of microwave scattering by raindrops," *Radio Science*, **15**, 1109–1119, 1980.

[21] Chang, H., and K. K. Mei, "Scattering of EM waves by buried or partly buried body of revolution," *IEEE Symposium on Antennas and Propagat.*, 653–656, 1981.

[22] Gupta, G. S., and A. Hizal, "Accounting for the tip scattering in radome analysis," *3rd Int. Conference on Antennas and Propagat., IEE*, 521–524, 1983.

[23] Fleming, A. H. J., *Numerical Analysis of Electromagnetic Scattering by Axisymmetric Inhomogeneous Composite Antenna Structures*, M. App. Sc. Thesis, Faculty of Technology, Chisholm Inst. of Tech., Caulfield, Australia, 1987.

[24] Morgan, M. A., *Numerical Computation of EM Scattering by Inhomogeneous Dielectric Bodies of Revolution*, Ph. D. Thesis, Dept. of Elec. Eng. and Comp. Sc., Univ. of California, Berkeley, Calif., 1976.

[25] Morgan, M. A., C. H. Chen, S. C. Hill, and P. W. Barber, "Finite element-boundary integral formulation for electromagnetic scattering," *Wave Motion*, North Holland, **6**, 91–103, 1984.

[26] King, R. W. P., and C. W. Harrison, Jr., *Antennas and Waves - A Modern Approach*, M.I.T. Press, Massachusetts, Chap. 4, 1969.

[27] Fleming, A. H. J., "Finite element solution to scattering from dielectrically loaded spheres," *Computational Techniques and Applications: CTAC-85*, Eds. J. Noye and C. Fletcher, North Holland, 763–774, 1986.

[28] Morgan, M. A., private communication, 1986.

[29] Lipitakis, E. A., "Generalized extended to the limit sparse factorization techniques for solving unsymmetric finite element systems," *Computing*, **32**, 255–270, 1984.